Hierarchical non-negative matrix factorization to characterize brain tumor heterogeneity using multi-parametric MRI

Nicolas Sauwen[1,2], Diana M Sima[1,2], Sofie Van Cauter[3], Jelle Veraart[4,5], Alexander Leemans[6], Frederik Maes[2,7], Uwe Himmelreich[8], Sabine Van Huffel[1,2]

[1] KU Leuven, Department of Electrical Engineering (ESAT), STADIUS Center for Dynamical Systems, Signal Processing and Data Analytics, Leuven, Belgium
[2] iMinds Medical IT
[3] Department of Radiology, University Hospitals of Leuven, Leuven, Belgium
[4] iMinds Vision Lab, Department of Physics, University of Antwerp, Antwerp, Belgium
[5] Center for Biomedical Imaging, Department of Radiology, New York University Langone Medical Center, New York, NY, USA
[6] Image Sciences Institute, University Medical Center Utrecht, Utrecht University, Utrecht, Netherlands
[7] KU Leuven, Department of Electrical Engineering (ESAT), Center for Processing Speech and Images, Leuven, Belgium
[8] Biomedical MRI/MoSAIC, Department of Imaging and Pathology, KU Leuven, Leuven, Belgium

Word count: *9331*

Keywords: *Multimodality imaging, Dynamic contrast methods, High order diffusion MR methods, Spectroscopic imaging, Head and neck cancer, Non-negative matrix factorization*

List of abbreviations: *ADC: apparent diffusion coefficient; aHALS: accelerated hierarchical alternating least squares; Cho: total choline; cMRI: conventional magnetic resonance imaging; Cre: total creatine; CSF: cerebro-spinal fluid; DKI: diffusion kurtosis imaging; DSC-MRI: dynamic susceptibility-weighted contrast-enhanced magnetic resonance imaging; DTI: diffusion tensor imaging; DWI: diffusion-weighted imaging; FA: fractional anisotropy; FLAIR: fluid-attenuated inversion recovery; FOV: field of view; FWHM: full width at half maximum; GBM: glioblastoma multiforme; Glx: glutamine+glutamate; Gly: glycine; ^{1}H-MRSI: proton magnetic resonance spectroscopic imaging; hNMF: hierarchical non-negative matrix factorization; Lac: lactate; Lip: lipids; MD: mean diffusivity; mI: myo-inositol; MK: mean kurtosis; MP-MRI: multi-parametric magnetic resonance imaging; NAA: N-acetyl-aspartate; NMF: non-negative matrix factorization; NNLS: non-negative linear least-squares; PWI: perfusion-weighted imaging; rCBV: relative cerebral blood volume; ROI: region of interest; T1+C: contrast-enhanced T1; VOI: volume of interest; WHO: World Health Organization*

Abstract

Advanced MRI modalities such as magnetic resonance spectroscopic imaging, perfusion-weighted imaging and diffusion-weighted imaging have shown their added value to characterize brain tumors and detect full tumor extent. Tissue characterization in brain tumors and in particular in high-grade gliomas is challenging due to the co-existence of several intra-tumoral tissue types within the same region and the high spatial heterogeneity. An accurate and reproducible method for brain tumor characterization and the detection of the relevant tumor substructures could be of great added value for the diagnosis, treatment planning and follow-up of individual patients. This study presents a hierarchical non-negative matrix factorization (hNMF) technique, providing tissue characterization on a voxel-by-voxel basis and incorporating the concept of tissue mixtures. Tissue-specific patterns are obtained and the spatial distribution of each tissue type is visualized by means of abundance maps. The hNMF algorithm is applied to multi-parametric MRI data of 13 glioma patients without necrosis

(tumor grades I, II and III) and 11 patients with necrosis (tumor grade IV). Dice-scores were calculated by converting the abundance maps into a tissue segmentation and comparing it to the manual segmentation by a radiologist. Correlation coefficients were calculated between the pathologic tissue sources and the average feature vector within the corresponding tissue region. For the patients without necrosis, an average Dice-score of 86% and an average correlation coefficient of 0.96 were found for the tumor region. For the patients with necrosis, average Dice-scores of 77%, 71% and 85% were obtained for active tumor, necrosis and the whole tumor region. The average correlation coefficients were 0.90 for active tumor and 0.97 for necrosis. hNMF was also applied to reduced MRI datasets, to show the added value of individual MRI modalities. hNMF can be applied on a patient-by-patient basis, providing a more refined tissue characterization compared to standard segmentation techniques.

Introduction

Neuro-imaging has become an indispensable tool when it comes to the diagnosis, treatment planning and follow-up of brain tumor patients. Conventional magnetic resonance imaging (cMRI) is the imaging modality of choice upon suspicion of a brain tumor. cMRI allows for localization of the lesion and assessment of radiological features like contrast enhancement and presence of necrosis, which might aid in establishing differential diagnosis. However, in a significant number of cases, cMRI is unable to provide reliable diagnosis and grading (1), which is crucial for optimal treatment planning and prognosis.

The international classification system published by the World Health Organization (WHO) based on histopathology is currently recognized as the gold standard for classifying brain tumors (2). Tumor grading is based on histological criteria such as cell density, nuclear atypia, mitosis, necrosis and endothelial proliferation. High-grade gliomas are known to show intra-tumoral heterogeneity, with spatial differences in cellular phenotype and malignancy grade (3,4). Due to this heterogeneity, there is a risk of underdiagnosing as biopsy sampling might not represent the most malignant part of the tumor (5). Intra-tumoral heterogeneity is not adequately reflected in cMRI (4), making it an improper tool for biopsy targeting. It is estimated that up to 25% of brain tumors are undergraded because the most malignant part of the tumor may not enhance after contrast administration (6).

Over the past decade, advanced MRI modalities, such as perfusion-weighted imaging (PWI), diffusion-weighted imaging (DWI) and MR spectroscopic imaging (MRSI) have gained interest in the clinical field, and their added value regarding brain tumor diagnosis, treatment planning and follow-up has been recognized (7).

PWI assesses the hemodynamics of brain tumors. More specifically, it proposes to measure the degree of tumor angiogenesis, and possibly capillary permeability, as the blood-brain barrier is disrupted in the newly-formed glioma microvessels. Relative cerebral blood volume (rCBV) is commonly accepted as the most suitable parameter for studying brain tumors (8). In astrocytomas, a strong correlation between rCBV and tumor grade has been reported (9,10), with rCBV values increasing along with the tumor grade. Nevertheless, there exists substantial intragrade variability of rCBV that increases with tumor grade. In addition, oligodendrogliomas may present with high rCBV regardless of grade (11). rCBV measurements in the peri-tumoral region have been shown to differentiate glioblastoma multiforme (GBM) from metastases, suggesting the detection of tumor infiltration (10,12). Furthermore, several studies have suggested that maximum tumoral rCBV might be an indicator of the most malignant part of the tumor for biopsy targeting (13,14).

Proton MRSI (^{1}H-MRSI) provides biochemical information regarding the spatial distribution of metabolites in a localized region of the brain. The principal metabolites found in brain tumors include lipids (Lip), lactate (Lac), N-acetyl-aspartate (NAA), glutamine+glutamate (Glx), total creatine (Cre), total choline (Cho), glycine (Gly) and myo-inositol (mI). Statistically significantly higher metabolite ratios of Cho/Cre and Cho/NAA have been reported in high-grade gliomas compared to low-grade gliomas (15). Lipids are a hallmark of necrosis, hence elevated Lip levels are seen almost exclusively in high-grade gliomas, particularly in GBMs (16). Nevertheless, considerable overlap between low- and high-grade glioma metabolite levels has been demonstrated. Sites with elevated levels of Cho or Cho/NAA have been proposed as biopsy targets and have been reported to increase the accuracy of tumor biopsy (17,18). MRSI measurements in peri-tumoral edema surrounding GBMs have shown increased Cho levels, suggesting tumor infiltration (12,19).

DWI aims at visualizing the mobility of water molecules within tissue due to Brownian motion. The apparent diffusion coefficient (ADC) relates to the mean path length of water diffusion within each tissue voxel (20). Several reports have shown that minimum ADC values correlate inversely with glioma grade, probably because of increasing tumor cellularity with increasing grade (21,22). Nevertheless, substantial overlap in ADC values among different grades limit its clinical applicability. Diffusion tensor imaging (DTI) is used to describe diffusion anisotropy. Two DTI metrics characterize the three-dimensional variability of the diffusion process: mean diffusivity (MD) and fractional anisotropy (FA) (23). Mixed results have been reported on the usage of DTI to detect tumor invasion in edema surrounding gliomas (24,25). Diffusion kurtosis imaging (DKI) is an extension of DTI, taking into account the non-Gaussian component of the diffusion process due to diffusion restriction or tissue heterogeneity. In isotropic tissue, this non-Gaussian diffusivity can be quantified by the mean kurtosis (MK) value (26). Furthermore, it has been demonstrated that DKI provided more accurate estimates of MD and FA than DTI (27). First results of using DKI for grading and differential diagnosis of brain tumors look promising (28,29).

The recent emergence of advanced MRI techniques has allowed us to learn much more about brain tumors in a non-invasive way. Many studies have investigated the potential of individual MRI modalities to characterize tumor grade, detect full tumor extent and assess early success of therapy. Although the added value of PWI, DWI and MRSI is unmistakable, it has become clear that no modality in itself is specific enough to answer these clinical questions unambiguously. This conclusion has led towards multi-parametric MRI (MP-MRI), i.e. the combination of several MRI modalities to provide complementary information on the structural, hemodynamic and/or biochemical characteristics of the tissue. Several studies have shown that MP-MRI improves diagnostic accuracy when it comes to grading gliomas compared to individual MRI modalities (7,15,30,31). Other studies have reported improved differentiation of intra-tumoral and peri-tumoral tissue types by applying supervised classification methods to MP-MRI data (32,33). Although the spatial heterogeneity of high-grade gliomas is partially explained by the presence of different stages of the disease throughout the lesion (3), it is also attributed to the co-existence of several intra-tumoral tissue types within the same region, such as the presence of focal necrosis within viable tumor tissue (34), tumor infiltration in peri-tumoral edema (12) and the formation of vasogenic edema in the active tumor region (35). Therefore, characterization of the tumoral and peri-tumoral tissue might benefit from a model that incorporates the concept of tissue mixtures. Blind source separation techniques have been applied to brain tumor MRSI data for this purpose. In particular, non-negative matrix factorization (NMF) methods have been shown to

give most promising results (36,37). NMF aims to extract physically meaningful sources, corresponding to tissue-specific patterns. It is an unsupervised technique, i.e. it can be applied on a patient-by-patient basis without the need for a large training dataset. NMF assesses the relative contribution of each tissue type within each voxel, assuming the dataset can be modelled as a linear combination of the constituent tissue types. In this study, a hierarchical NMF technique is presented and applied to an MP-MRI dataset combining cMRI, PWI, ^{1}H-MRSI and DKI to characterize tumor heterogeneity, providing a comprehensive representation of the spatial distribution of tissue types within and surrounding the tumor. Although voxels of mixed tissue contributions are allowed, the method benefits from the assumption that a large number of voxels will contain mainly one tissue type, given the relatively high resolution of cMRI, at which all MRI maps are resampled. Tissue-specific patterns are obtained on a patient-by-patient basis. The usage of MP-MRI data provides a detailed tissue characterization and delimitation at the cMRI voxel level, and is able to improve source separation of the different tissue types. To assess the added value of individual MRI modalities, hNMF is also applied to reduced MP-MRI datasets, leaving out one modality at a time, and to cMRI data only.

Methodology

Patient population

The institutional human ethics review board approved this prospective study. Written informed consent was obtained from every patient before participation. We examined 24 patients with suspicion of glioma based on conventional radiological imaging, prior to any treatment (9 females/15 males; age range: 22–78 years, median age: 55 years). We enrolled 13 patients with a high-grade glioma, of whom 11 had grade IV glioma (GBM) and 2 had grade III glioma. Ten patients with a low-grade glioma were recruited. Of these 10 patients, 1 was diagnosed with a diffuse fibrillary glioma grade II, 3 with a grade II astrocytoma, 2 with a grade II oligodendroglioma, 1 with a grade II oligoastrocytoma, 1 with a grade II lesion with mixed findings of pilocytic astrocytoma, angiocentric glioma, and oligodendroglioma, and 2 with grade I oligodendroglioma. One patient had a grade II astrocytoma with focal progression to a grade III glioma. The lesions were classified according to grade using the 2007 WHO classification (2), with histopathological confirmation in all cases.

Data acquisition and analysis

MRI acquisition was performed on a 3T MR system (Philips Achieva, The Netherlands), using a body coil for transmission and an 8-channel head coil for signal reception. The total scanning time for all MRI modalities was 45min.

cMRI

An axial spin echo T2-weighted MRI was acquired with the following parameters: repetition time (TR)/ echo time (TE): 3000/80ms; slice/gap: 4/1 mm; turbo factor: 10; field of view [FOV]: 230×184mm^2; acquisition matrix: 400×300.

A T1-weighted 3D spoiled gradient echo MRI scan with contrast administration was performed with the following parameters: fast field echo, TR/TE/inversion time (TI): 9.7/4.6/900ms; flip angle: 8°; turbo field echo factor: 180; acquisition voxel size: 0.98×0.98×1mm^3; 118 contiguous partitions.

An axial FLAIR MRI scan was acquired with the following parameters: TR/TE/TI: 11000/120/2800 msec, slice/gap: 4/1 mm, FOV: 230×184mm², acquisition matrix: 240×134.

PWI

Perfusion images were obtained using Dynamic Susceptibility-weighted Contrast-enhanced (DSC) MRI with a gradient-echo EPI sequence: TR/TE: 1350/30ms; section thickness/gap: 3/0mm; dynamic scans: 60; FOV: 200×200mm^2; matrix: 112×109; scan time: 1min26s. EPI data were acquired during the first pass following a rapid injection of a 0.1mmol/kg body weight bolus of meglumine gadoterate (Dotarem, Guerbet, France) via a mechanical pump at a rate of 4mL/s, followed by a 20-mL bolus of saline.

DSC data were analyzed using the DSCoMAN plugin (38) in ImageJ (39). rCBV maps were derived from the dynamic signal intensity curves using the method proposed by Boxerman et al. (40). To correct for contrast agent leakage, the relaxivity-time curve in each voxel is approximated as a linear combination of the whole-brain average curve in the non-enhancing voxels and its time integral, with the first term representing the uncontaminated relaxivity change and the second term reflecting the effect of leakage. The coefficients of this linear combination are found in each voxel using linear least-squares fitting.

MRSI

A 2D-^{1}H MRSI protocol was used as previously described (41). A point-resolved spectroscopy sequence was used as the volume selection technique with a bandwidth of 1.3kHz for the conventional slice-selective pulses; TR/TE: 2000/35ms; FOV: 160×160mm^2; maximal volume of interest (VOI): 80×80mm^2; section thickness: 10mm; acquisition voxel size: 10×10mm^2; reconstruction voxel size: 5×5mm^2; receiver bandwidth: 2000Hz; samples: 2048; number of signal averages: 1; water suppression method: multiple optimizations insensitive suppression train (42); first- and second-order pencil beam shimming; parallel imaging: sensitivity encoding with reduction factors of 2 (left-right) and 1.8 (anterior-posterior); scan time: 3min30s. Automated pre-scanning optimized the shim in order to yield a peak width consistently under 20Hz full-width half-maximum (FWHM). The slice was positioned in the center of the tumor.

The raw MRSI data were exported from the Philips platform after standard post-processing (zero-filling in k-space, transformation from k-space to time domain, automatic phase correction and eddy current correction). Further processing was done with the in-house SPID software (43) in MatLab 2012b (MathWorks, Massachussets, USA). AQSES-MRSI (44) was used to quantify the following metabolites using an experimentally acquired metabolite basis set: Lip at 1.3ppm, Lac, NAA, Glx, Cre, Cho, mI and Gly. MPFIR (Maximum-Phase Finite Impulse Response) filtering(45) was included in the AQSES-MRSI procedure for residual water suppression: the model order was set to 25 and the spectral range from 0.25 to 4.2ppm. A band of voxels at the outer edges of the VOI was omitted to avoid chemical shift displacement artifacts and lipid contamination (band proportional to the grid size, maximally 3 voxels wide for a 16×16 grid).

DKI

An EPI DWI sequence with a spin-echo readout was used to acquire the DKI data, according to an optimized DKI protocol (26). Implemented b-values were 0, 700, 1000, and 2800s/mm^2, applied in respectively 10, 25, 40, and 75 uniformly distributed directions. The following parameters were used throughout the DKI acquisition sequence: TR/TE: 3200/90ms; gradient

duration/diffusion time interval: 20/48.3ms; FOV: 240×240mm^2; matrix: 96×96; number of signal averages: 1; section thickness/gap: 2.5/0mm; parallel imaging: SENSE with factor 2 in the antero-posterior direction. The scan time was 17min30s.

After motion and Eddy current correction (46), isotropic smoothing was applied using a Gaussian kernel (FWHM=3mm) to reduce Gibbs ringing. However, smoothing was applied to the b=0 and b=700 images only, so as not to alter the nature of the noise distribution in the highly diffusion-weighted images in order to avoid a noise bias in the subsequent tensor estimation (47). Diffusion and kurtosis tensors were estimated in each voxel using a constrained weighted linear least-squares algorithm (47). MD, FA and MK maps were derived from the tensors according to (26,48).

Data coregistration

All MRI datasets were coregistered and brought to the same spatial resolution to perform voxelwise analysis. Cubic spline interpolation was used to create an interpolated set of T1+C images, with one slice coinciding with the central plane of the MRSI VOI. Only the MRI data of this central slice within the MRSI region of interest (ROI) were considered for hNMF analysis, as no MRSI data were available outside of this ROI. Skull-stripping was applied to all images prior to coregistration. The cMRI datasets and the PWI dataset were rigidly coregistered to the interpolated T1+C reference set using SPM (49). The normalized mutual information criterion was used for coregistration (50), with cubic spline interpolation for reslicing. A nonlinear coregistration of the diffusion-weighted parameter maps to the coregistered T2-weighted MRI dataset was performed using ExploreDTI (51) to minimize the local misalignment between the EPI distorted DKI data and the cMRI data. The MRSI data were spatially aligned with the reference set and resampled using cubic spline interpolation, assuming no patient motion with respect to the reference. T1+C was acquired closest to MRSI within the entire scanning protocol, minimizing the risk of patient motion between the MRSI dataset and the reference set. All MRI parameters were brought to the spatial resolution of the original T1+C dataset, i.e. 0.98×0.98×1mm^3.

Hierarchical Non-Negative Matrix Factorization

NMF is a blind source separation technique (52), in which a matrix X is approximately factorized into the product of a source matrix W and an abundance matrix H:

$$X_{n\times m} \approx W_{n\times r} \times H_{r\times m} \quad [1]$$

X contains a set of non-negative data, with m data points on its columns and n features per data point on its rows. The columns of W represent the r sources. H contains per column the abundance of each of the r sources for one particular data point. In this way, NMF describes each point in a dataset by a linear combination of a predefined number of sources. Characterization of the tumor heterogeneity based on MP-MRI can be seen as an NMF-problem as follows: for each voxel within the MRSI ROI (as only this subset of voxels has a full MP-MRI dataset), the corresponding MRI features are stacked in a vector. The obtained vectors are then grouped as columns of a matrix X, such that each column of X represents a set of MRI features for one particular voxel. Such a feature set can then be approximated as a linear mixture of a certain number of tissue types, each of which is characterized by a tissue-specific pattern. NMF is an unsupervised learning method, meaning that it can be applied on a patient-by-patient basis.

The mathematical formulation of the basic NMF problem to perform the factorization in Equation[1] is given by:

$$\min_{W,H} f(W,H) = \frac{1}{2}\left\|X - WH\right\|_F^2 \quad [2]$$

such that: $\forall i, j:\ W_{i,j}, H_{i,j} \geq 0$

In our study the accelerated hierarchical alternating least squares (aHALS) NMF implementation was used (53). aHALS was proven superior to other NMF implementations in a study to characterize brain tumors using simulated MRSI data (54).

The MRI parameters discussed in the previous section were used as input features: T2, T1+C, FLAIR, rCBV, Lip, Lac, NAA, Glx, Cre, Cho, mI, Gly, MD, FA and MK. To all non-metabolic MRI maps, smoothing was applied using moving average windows with kernel sizes of 3×3 of 5×5. These smoothed MRI maps were also added to the feature set, resulting in a total of 29 features (8 metabolic features, 7 non-metabolic features and 14 smoothed non-metabolic features). The metabolic features were rescaled by dividing them by the maximum metabolite value throughout the MRSI ROI, such that relative amplitudes were unchanged between the different metabolites. For the non-metabolic features, each feature's full range was rescaled to [0 1].

The hNMF procedure consists of three steps. Fig.1 gives a schematic overview of the hNMF procedure and the individual steps are discussed in detail below.

Step1

A rank-2 NMF analysis is performed on all voxels in the MRSI ROI, resulting into 2 sources and their corresponding abundance maps (H-maps). Under the assumption that pathologic and normal tissue are present in the ROI, one of the sources contains the pathologic tissue (active tumor and possibly necrosis and edema), while the other source contains normal brain tissue (white matter, gray matter, cerebro-spinal fluid (CSF), blood vessels,...). As NMF suffers from scaling and permutation ambiguities, each H-map's maximum value was rescaled to 1 and the sources were rescaled accordingly.

Step2

Tissue-specific patterns are derived by applying a second level of NMF to the pathologic tissue region and to the normal tissue region. The number of tissue types present in the MRSI ROI is not *a priori* known, as it depends on the characteristics of the tumor and the location of the MRSI ROI. The number of tissue types required for each region was found empirically, by considering the pathologic and the normal abundance maps in combination with the cMRI data. As there is no clear boundary between the pathologic and the normal region, and voxels at the interface of both regions will contain significant abundances from both sources, it is not initially clear which voxels to consider in each region. An iterative procedure is used to consider different masks for both tissue regions. The voxelwise ratios of the pathologic and the normal abundance to their sum, H_{ratio1} and H_{ratio2}, are calculated over the whole ROI:

$$H_{i,ratio1} = \frac{H_{i,pathologic}}{H_{i,normal} + H_{i,pathologic}} \quad [3] \qquad \text{and} \qquad H_{i,ratio2} = \frac{H_{i,normal}}{H_{i,normal} + H_{i,pathologic}} \quad [4]$$

with index *i* referring to voxel *i*. We then consider a variable threshold *t* to define a mask on the H_{ratio1} and H_{ratio2} map. At each fixed value of *t*, NMF is applied to the group of voxels with H_{ratio1} larger than *t* for the pathologic region and to the group of voxels with H_{ratio2} larger than *t* for the normal region. We let *t* range from 0.5 to 1, with *t*=0.5 corresponding to voxels with equal abundances for the pathologic and the normal source and *t*=1 corresponding to voxels with a nonzero abundance for only one of the sources. As *t* increases, only voxels that have a clear dominance of either source are withheld for the second level of NMF. In this way, pathologic tissue types do not have to fit voxels that contain significant contributions of normal tissue, and vice-versa. The *t*-interval was divided into 20 steps, as a finer step size did not significantly improve the results any further.

Step3

The tissue-specific patterns obtained from the pathologic and the normal region for each value of *t* are then re-combined to calculate the abundance of all tissue types over the whole ROI using NNLS (55). To find the optimal threshold value *t,* which will correspond to the final hNMF factorization, a criterion that promotes sparsity among the intra-voxel tissue abundances is introduced. The optimal threshold *t* then corresponds to the highest H^t_{ratio3} value, where:

$$H^t_{ratio3} = \sum_i \frac{H^t_{i,\max}}{\sum_j H^t_{i,j}} \quad [5]$$

with $H^t_{i,j}$ denoting the abundance of source *j* in voxel *i* after the second level of NMF at threshold *t* and $H^t_{i,\max}$ denoting the highest abundance in voxel *i* at threshold *t*. In [5], the summation over *i* covers the whole ROI and the sum in the denominator goes over all the sources *j*. A higher value of H^t_{ratio3} can be interpreted as a more sparse solution: on average, the voxels will have a more dominant tissue type. For each NMF analysis, the W- and H-matrix were initialized randomly. As NMF is a non-convex optimization problem, the full hNMF procedure was repeated 20 times for each patient, and the output with the highest H_{ratio3} was withheld.

As a measure of reliability of the hNMF result, an error map is computed, quantifying the modeling error in each voxel:

$$E_i = \left\| X_i - WH_i \right\|_2 \quad [6]$$

with E_i being the modeling error in voxel *i*, and X_i and H_i the ith columns of matrices *X* and *H*, respectively. The error map allows visual detection of badly fitted regions, for instance due to the presence of outliers, bad quality data or an insufficient number of tissue sources.

To verify the robustness of the hNMF algorithm when less MRI modalities are acquired, hNMF was also applied to reduced feature sets, leaving out all MRI parameters belonging to one MRI modality. Reduced feature sets were considered by omitting consecutively cMRI, PWI, MRSI and DKI data, respectively. hNMF was also applied to the cMRI data only, allowing to assess the added value of using MP-MRI data.

Validation

Abundance maps
For each patient, a tissue segmentation was obtained from the abundance maps, assigning each voxel to 1 tissue class. This was done by applying k-means clustering (55) to the *H*-values, with *k* set to the number of tissue types resulting from hNMF. The tumor region (and for GBMs also the necrotic region) obtained from hNMF was compared to the manual segmentation by a radiologist (with 6 years of experience in brain tumor research) using the Dice score:

$$Dice_{tissue} = 2 \times \frac{A_{tissue,hNMF} \cap A_{tissue,radiol}}{A_{tissue,hNMF} \cup A_{tissue,radiol}} \quad [7]$$

with $A_{tissue,hNMF}$ the area of the tissue region as defined by hNMF and $A_{tissue,radiol}$ the area as defined by the radiologist. Dice-scores are reported for the tumor region for gliomas without necrosis (grades I, II and III) and for active tumor, necrosis and the whole tumor region (active tumor+necrosis) for gliomas with necrosis (GBMs, grade IV).

Tissue sources
The validation of the sources is based on the hypothesis that the sources correspond to actual tissue types. The average feature vector was calculated over all voxels belonging to the same tissue type, based on the radiologist's segmentation. Correlation coefficients were calculated between the normalized average feature vector and the corresponding normalized source obtained from hNMF. Correlation values were calculated for the tumor region for the gliomas without necrosis and for the active tumor and the necrotic region for GBMs.

Results

An illustration of the hNMF analysis for a GBM patient is given below: some relevant MRI features are shown in fig.2 and the results of the hNMF analysis are shown in fig.3. Five different tissue types were characterized by hNMF within the MRSI ROI: active tumor, necrosis, edema, blood vessels and white matter. The detailed hNMF analysis results of all patients can be found in 'Supplementary materials'.

Table 1 reports the average, standard deviation and range of the Dice-scores for the tumor region of the glioma patients without necrosis for all considered datasets. An average Dice-score of 86% was found for the full MP-MRI dataset, indicating good agreement between the manual segmentation by the radiologist and the segmentation derived from hNMF. The average Dice-score decreased to 84%, 84% and 83% when omitting PWI, MRSI and DKI, respectively. Only when omitting cMRI, a larger decrease in performance was found with an average Dice-score of 75%. When considering only the cMRI data, the average Dice-score was still 81%.

Table 2 reports the average, standard deviation and range of the correlation coefficients for the tumor region of the glioma patients without necrosis for all considered datasets. For the full MP-MRI dataset, an average correlation coefficient of 0.96 was found, with correlation coefficients above 0.90 for all patients except one. These high correlation values confirm that the tumor source can indeed be considered as a tissue-specific pattern for the tumor tissue. When considering the reduced MP-MRI datasets and the cMRI dataset, similar average

correlation coefficients are found, with even slightly increased values of 0.97, 0.98 and 0.98 when leaving out PWI, MRSI and DKI, respectively.

Table 3 shows the Dice-scores for the active tumor, the necrotic and the whole tumor region of the GBM patients for all considered datasets. For the full MP-MRI dataset, average Dice-scores of 77%, 71% and 85% were found for active tumor, necrosis and the whole tumor region, respectively. For active tumor, a decrease in the average Dice-score of 14%, 5%, 9% and 1% was found when omitting cMRI, PWI, MRSI and DKI, respectively. When considering only cMRI data, an average decrease of 10% was obtained. For the necrotic region, there is an average decrease of 14%, 3%, 5% and 4% when omitting cMRI, PWI, MRSI and DKI, respectively, and of 23% for cMRI data only. The necrotic area within the MRSI ROI was small for patients 15 and 23, resulting in significant contamination from other tissue types and a lower Dice-score for necrosis. In general, a wider range and a higher standard deviation was found for necrosis compared to active tumor. For the whole tumor region, the average Dice-score decreased by 8%, 5%, 7% and 3% when omitting cMRI, PWI, MRSI and DKI, respectively, and by 16% for cMRI data only.

Table 4 reports the average, standard deviation and range of the correlation coefficients for the active tumor region, necrosis and the whole tumor region of the GBM patients for all considered datasets. For the full MP-MRI dataset, the average correlation coefficient for active tumor was 0.90, which is lower compared to the patients without necrosis. This lower correlation coefficient could be explained by the significant abundance of necrosis within the active tumor region that was found in many GBM patients. Such non-negligible abundance of necrosis within the active tumor region is explained by the presence of very small focal necrosis which is not manifesting on cMRI and commonly found in those patients. For necrosis, an average correlation coefficient of 0.97 was found for the full MP-MRI dataset. When considering the reduced MP-MRI datasets, the average correlation coefficient for active tumor decreased by 0.03 and 0.07 without PWI and MRSI, respectively, and increased by 0.01 and 0.05 without cMRI and DKI, respectively. For the cMRI dataset, there was an average decrease of 0.05 compared to full MP-MRI. For necrosis, we found a decrease of the average correlation coefficient by 0.05, 0.01 and 0.01 without cMRI, MRSI and DKI, respectively, and no change without PWI. For cMRI data only, a decrease of 0.04 was found.

Discussion

Unsupervised vs supervised classification

Given the wide range of tumor characteristics that is reported for high-grade gliomas and the large heterogeneity that is often seen within the same lesion, unsupervised methods have the advantage of not making any prior assumptions about the expected values of the individual features. This has allowed us to apply hNMF on a patient-by-patient basis, resulting in patient-specific tissue patterns. Given the large variability that was found in the GBM tumor sources, a patient-specific approach seems preferential for the MP-MRI data. Several studies have applied supervised classification methods to characterize brain tumor substructures. Di Costanzo et al. applied linear discriminant analysis to MP-MRI data to perform ROI based classification of solid tumor, edema, edema/tumor and infiltrated peri-tumoral tissue on low- and high-grade gliomas (33). Classification accuracy of 67% was found for solid tumor ROIs. Another study used support vector machines on a combination of cMRI and DTI to distinguish enhancing tumor, non-enhancing tumor and edema in high-grade brain tumors (32). Voxelwise classification rates of 89% and 34% were found for enhancing and non-

enhancing tumor, respectively. As was pointed out in the latter study, tumor regions might contain varying degrees of neoplasm combined with healthy tissue or edema. In the current study, GBMs showed varying degrees of diffusion restriction and lipid content in the active tumor region, which is partly explained by the presence of focal necrosis. Identifying tissue-specific patterns across patients is hampered due to the co-existence of different tissue types, especially when mixed tissue classes are considered. This aspect of tissue complexity is not taken into consideration by supervised classification methods. Furthermore, unsupervised methods do not require data normalization, which can be subjective and time consuming, and they have no need for a uniform training dataset.

Tumor segmentation

Tumor segmentation is a challenging task in the image analysis of brain tumors. Manual delineation is still the gold standard for brain tumors in clinical practice. Nevertheless, it is a time-consuming and user-dependent process, prone to errors and with questionable reproducibility (56). To overcome these limitations, many sophisticated algorithms have been developed for automated segmentation. However, few have achieved the speed, accuracy, and limited user interaction required for routine clinical use (57). One means of validation was to convert the hNMF results into an absolute voxel-by-voxel segmentation, by applying k-means clustering to the obtained abundance maps. Comparing the hNMF-based segmentation to the manual segmentation by an experienced radiologist, average Dice-scores for the whole tumor region of 86% and 85% were found for the glioma patients without and with necrosis, respectively. For the GBMs, average Dice-scores of 77% and 71% were found for the active tumor region and for the necrotic region, respectively. These Dice-scores are higher than the average Dice-scores of the best performing methods reported in (58). It must be noted that these methods are all supervised classification methods which only rely on cMRI data. Nevertheless, it shows that our results are competitive with the state-of-the-art segmentation techniques. We have thus shown that the hNMF method presented in this study can be applied as a valid unsupervised segmentation technique.

The hNMF method provides tissue characterization that goes beyond standard segmentation of individual voxels. The relative contribution of each tissue type within each voxel is presented by means of the abundance maps. These maps allow direct visual interpretation of the hNMF results, combining the information of all MRI parameters into one map per tissue type. The relative contributions of different tissue types within the tumor region provide us with more insight in the spatial heterogeneity of the tumor. To further synthesize visual assessment, the abundance maps can be combined into a single nosologic image, in which each tissue class is represented by one colour and colour mixtures are used to quantify the relative contribution of each tissue type in each voxel (59,60).

Comparison with previous NMF studies

To the authors' knowledge, this is the first study in which hNMF is applied to multi-parametric MRI data for brain tumor characterization. Several studies have applied NMF to brain tumor MRSI data for tissue differentiation (36,37,61). A hierarchical implementation was used because previous results have shown that hNMF outperforms one-level NMF when it comes to brain tumor characterization (62). The advantage of using MP-MRI data compared to only MRSI data is twofold. Firstly, the higher resolution of the added MRI features will allow a more detailed and accurate delineation of the tumor subregions. Previous studies also considered an hNMF-based segmentation for validation purposes. In Li et al.(62), this validation was only done visually, hampering comparison of the results. Ortega-Martorell et al.(37) did quantify the correspondence between the segmentation obtained from hNMF and

post-mortem Ki67 immunostaining applied to 7 GBM bearing mice, resulting in a mean accuracy of 83.7% for the tumor region. However, safe thresholds were applied to the proliferation index obtained from immunostaining for labelling the voxels, such that MRSI voxels near the tumor-normal tissue interface were not always considered. Furthermore, differentiation between active tumor and necrosis was not considered. Secondly, the low resolution of the MRSI data results in considerable partial volume effects, with many voxels containing tissue mixtures. Especially in the case of small lesions, there might not be any pure voxels containing only necrosis or active tumor, which will make source separation more difficult. Additionally, it was pointed out in (62) that the MRSI spectrum of the tumor source can approximately be modelled as a linear combination of the necrotic and the normal tissue source. This complicates the separability of the tissue types. Adding other MRI features to the dataset will further decorrelate the tissue sources, improving their separability.

The H_{ratio3} criterion that was implemented to find the optimal threshold t in hNMF step3 assumes that most voxels will contain mainly one tissue type. However, when only MRSI data are considered, it is not evident that the same criterion can be applied successfully, given the low spatial resolution of the MRSI data. By applying the optimal threshold t to both the H_{ratio1} and H_{ratio2} map, voxels that contain considerable contributions of both the pathologic and the normal source after step1 are not considered for determining the tissue-specific patterns in hNMF step2. Since in step2, each voxel is fully modelled by either the pathologic or the normal sources, these mixed voxels will act as a confounding factor for determining the tissue sources. Omitting these voxels for the source determination will result in a better source separation. In previous hierarchical schemes, all voxels were always considered for determining the tissue-specific patterns in hNMF step2 (36,61,62). To cope with the large difference in spatial resolution among the MRI modalities, we brought all modalities to the spatial resolution of the T1+C reference dataset and we added smoothed versions of all non-metabolic maps by applying 3×3 and 5×5 averaging windows. This approach seemed an optimal trade-off to keep maximal imaging information and at the same time bridge the large gap in spatial resolution. In previous NMF studies of brain tumors, no distinction was made between the different normal brain tissue types. Especially in the case of MP-MRI data, more detailed information is available to also distinguish between different normal brain tissues. In fact, we obtained inferior validation results and more contamination between tissue types when only one 'normal' tissue class was considered.

Reduced MP-MRI datasets and cMRI only

The hNMF procedure was also applied to reduced feature sets, leaving out one MRI modality at a time. Compared to the full MP-MRI dataset, a decrease in the average Dice-score was found for all reduced feature sets and in each pathologic region. The average correlation coefficient showed a less distinct decrease in most cases and even a slight increase in some cases. It must be noted that a higher correlation coefficient does not warrant better performance: a significant amount of voxels will not contain purely one tissue type, such that the average feature vector per region is expected to contain some contamination from other tissue types. For the patients without necrosis, the average Dice-score decreased by 2% without PWI and MRSI and by 3% without DKI. A larger decrease of 11% was found when omitting cMRI. For the GBM dataset, the average Dice-score decreased by no more than 5% in any pathologic region without PWI or DKI. When MRSI data are left out, average Dice-scores decreased by 9% for active tumor, 5% for necrosis and 7% for the whole tumor region. When omitting cMRI, the average Dice-score decreased by 14% for necrosis, 14% for active tumor and 8% for the whole tumor region. The larger decrease for the subregions compared to the whole tumor region indicates that it becomes particularly more difficult to distinguish

active tumor from necrosis when cMRI data are excluded. It has been demonstrated that the hNMF protocol still performs well when reduced MP-MRI feature sets are considered. hNMF can easily deal with whichever MRI dataset is available on an individual patient basis, making it robust when not all input features are available.

We also applied hNMF to the cMRI dataset only, to assess the added value of using MP-MRI data. For the patients without necrosis, an average Dice-score of 81% was found, which is 5% lower compared to the full MP-MRI dataset. For the GBM patients, a larger decrease in average Dice-score was found in all pathologic regions: 10% for active tumor, 23% for necrosis and 16% for the whole tumor region. The added value of using MP-MRI data has thus been shown, particularly to characterize tumor heterogeneity in high-grade patients.

Voxelwise vs ROI analysis

Previous advanced MRI studies have often considered single statistical values for a lesion, or for a few ROIs within the lesion. Given the heterogeneous nature of high-grade gliomas, a simple statistical metric such as the mean value is inadequate in characterizing the whole tumor. Numerous studies have proposed minimum or maximum values of PWI, DWI or MRSI parameters to assess tumor malignancy (9,30,31) or to detect the most malignant part of the lesion for biopsy targeting (17,63). Such methods, although they have shown statistical significance in most cases, lack robustness against outlier values and have limited interpretability. A more detailed intra-tumoral tissue characterization will allow us to move towards more personalized and dedicated treatment planning.

Acknowledgements

This work has been funded by the following projects: Flemish Government FWO project G.0869.12N (Tumor imaging); IWT IM 135005; Belgian Federal Science Policy Office: IUAP P7/19/ (DYSCO, `Dynamical systems, control and optimization', 2012-2017); Henri Benedictus Fellowship of the Belgian American Educational Foundation; Interuniversity Attraction Poles Program (P7/11) initiated by the Belgian Science Policy Office. VIDI Grant 639.072.411 from the Netherlands Organisation for Scientific Research (NWO). EU: European Research Council under the European Union's Seventh Framework Programme (FP7/2007-2013), ERC Advanced Grant: BIOTENSORS (n°339804) and the EU MC ITN TRANSACT 2012 (n°316679).

References

1. Grant R. Overview: Brain tumour diagnosis and management/Royal College of Physicians guidelines. J. Neurol. Neurosurg. Psychiatry 2004;75 Suppl 2:ii18–23.

2. Louis DN, Ohgaki H, Wiestler OD, Cavenee WK, Burger PC, Jouvet A, Scheithauer BW, Kleihues P. The 2007 WHO classification of tumours of the central nervous system. Acta Neuropathol. (Berl.) 2007;114:97–109.

3. Paulus W, Peiffer J. Intratumoral histologic heterogeneity of gliomas. A quantitative study. Cancer 1989;64:442–7.

4. Jacobs AH, Kracht LW, Gossmann A, Rüger MA, Thomas AV, Thiel A, Herholz K. Imaging in neurooncology. NeuroRx J. Am. Soc. Exp. Neurother. 2005;2:333–47.

5. Jackson RJ, Fuller GN, Abi-Said D, Lang FF, Gokaslan ZL, Shi WM, Wildrick DM, Sawaya R. Limitations of stereotactic biopsy in the initial management of gliomas. Neuro-Oncol. 2001;3:193–200.

6. Earnest F, Kelly PJ, Scheithauer BW, Kall BA, Cascino TL, Ehman RL, Forbes GS, Axley PL. Cerebral astrocytomas: histopathologic correlation of MR and CT contrast enhancement with stereotactic biopsy. Radiology 1988;166:823–7.

7. Van Cauter S, De Keyzer F, Sima DM, Croitor Sava AR, D'Arco F, Veraart J, Peeters R, Leemans A, Van Gool S, Wilms G, Demaerel P, Van Huffel S, Sunaert S, Himmelreich U. Integrating diffusion kurtosis imaging, dynamic susceptibility-weighted contrast-enhanced MRI, and short echo time chemical shift imaging for grading gliomas. Neuro-Oncol. 2014;16:1010–1021.

8. Cha S, Knopp EA, Johnson G, Wetzel SG, Litt AW, Zagzag D. Intracranial mass lesions: dynamic contrast-enhanced susceptibility-weighted echo-planar perfusion MR imaging. Radiology 2002;223:11–29.

9. Sugahara T, Korogi Y, Kochi M, Ikushima I, Hirai T, Okuda T, Shigematsu Y, Liang L, Ge Y, Ushio Y, Takahashi M. Correlation of MR imaging-determined cerebral blood volume maps with histologic and angiographic determination of vascularity of gliomas. AJR Am. J. Roentgenol. 1998;171:1479–86.

10. Bulakbasi N, Kocaoglu M, Farzaliyev A, Tayfun C, Ucoz T, Somuncu I. Assessment of diagnostic accuracy of perfusion MR imaging in primary and metastatic solitary malignant brain tumors. AJNR Am. J. Neuroradiol. 2005;26:2187–99.

11. Young GS. Advanced MRI of adult brain tumors. Neurol. Clin. 2007;25:947–73, viii.

12. Law M, Cha S, Knopp EA, Johnson G, Arnett J, Litt AW. High-grade gliomas and solitary metastases: differentiation by using perfusion and proton spectroscopic MR imaging. Radiology 2002;222:715–21.

13. Lupo JM, Cha S, Chang SM, Nelson SJ. Dynamic susceptibility-weighted perfusion imaging of high-grade gliomas: characterization of spatial heterogeneity. AJNR Am. J. Neuroradiol. 26:1446–54.

14. Maia ACM, Malheiros SMF, da Rocha AJ, Stavale JN, Guimaraes IF, Borges LRR, Santos AJ, da Silva CJ, de Melo JGSP, Lanzoni OP, Gabbai AA, Ferraz FAP. Stereotactic biopsy guidance in adults with supratentorial nonenhancing gliomas: role of perfusion-weighted magnetic resonance imaging. J. Neurosurg. 2004;101:970–6.

15. Law M, Yang S, Wang H, Babb JS, Johnson G, Cha S, Knopp EA, Zagzag D. Glioma grading: sensitivity, specificity, and predictive values of perfusion MR imaging and proton MR spectroscopic imaging compared with conventional MR imaging. AJNR Am. J. Neuroradiol. 24:1989–98.

16. Kuesel AC, Sutherland GR, Halliday W, Smith IC. 1H MRS of high grade astrocytomas: mobile lipid accumulation in necrotic tissue. NMR Biomed. 1994;7:149–55.

17. Wagner M, Nafe R, Jurcoane A, Pilatus U, Franz K, Rieger J, Steinbach JP, Hattingen E. Heterogeneity in malignant gliomas: a magnetic resonance analysis of spatial distribution of metabolite changes and regional blood volume. J. Neurooncol. 2011;103:663–72.

18. Hall WA, Martin A, Liu H, Truwit CL. Improving diagnostic yield in brain biopsy: coupling spectroscopic targeting with real-time needle placement. J. Magn. Reson. Imaging JMRI 2001;13:12–5.

19. Ricci R, Bacci A, Tugnoli V, Battaglia S, Maffei M, Agati R, Leonardi M. Metabolic findings on 3T 1H-MR spectroscopy in peritumoral brain edema. AJNR Am. J. Neuroradiol. 2007;28:1287–91.

20. Le Bihan D. Apparent diffusion coefficient and beyond: what diffusion MR imaging can tell us about tissue structure. Radiology 2013;268:318–22.

21. Bulakbasi N, Guvenc I, Onguru O, Erdogan E, Tayfun C, Ucoz T. The added value of the apparent diffusion coefficient calculation to magnetic resonance imaging in the differentiation and grading of malignant brain tumors. J. Comput. Assist. Tomogr. 28:735–46.

22. Kitis O, Altay H, Calli C, Yunten N, Akalin T, Yurtseven T. Minimum apparent diffusion coefficients in the evaluation of brain tumors. Eur. J. Radiol. 2005;55:393–400.

23. Basser PJ, Mattiello J, LeBihan D. MR diffusion tensor spectroscopy and imaging. Biophys. J. 1994;66:259–67.

24. Lu S, Ahn D, Johnson G, Cha S. Peritumoral diffusion tensor imaging of high-grade gliomas and metastatic brain tumors. AJNR Am. J. Neuroradiol. 2003;24:937–41.

25. Provenzale JM, McGraw P, Mhatre P, Guo AC, Delong D. Peritumoral brain regions in gliomas and meningiomas: investigation with isotropic diffusion-weighted MR imaging and diffusion-tensor MR imaging. Radiology 2004;232:451–60.

26. Poot DHJ, den Dekker AJ, Achten E, Verhoye M, Sijbers J. Optimal experimental design for diffusion kurtosis imaging. IEEE Trans. Med. Imaging 2010;29:819–29.

27. Veraart J, Poot DHJ, Van Hecke W, Blockx I, Van der Linden A, Verhoye M, Sijbers J. More accurate estimation of diffusion tensor parameters using diffusion Kurtosis imaging. Magn. Reson. Med. Off. J. Soc. Magn. Reson. Med. Soc. Magn. Reson. Med. 2011;65:138–145.

28. Van Cauter S, Veraart J, Sijbers J, Peeters RR, Himmelreich U, De Keyzer F, Van Gool SW, Van Calenbergh F, De Vleeschouwer S, Van Hecke W, Sunaert S. Gliomas: diffusion kurtosis MR imaging in grading. Radiology 2012;263:492–501.

29. Raab P, Hattingen E, Franz K, Zanella FE, Lanfermann H. Cerebral gliomas: diffusional kurtosis imaging analysis of microstructural differences. Radiology 2010;254:876–81.

30. Fellah S, Caudal D, De Paula AM, Dory-Lautrec P, Figarella-Branger D, Chinot O, Metellus P, Cozzone PJ, Confort-Gouny S, Ghattas B, Callot V, Girard N. Multimodal MR imaging (diffusion, perfusion, and spectroscopy): is it possible to distinguish oligodendroglial tumor grade and 1p/19q codeletion in the pretherapeutic diagnosis? AJNR Am. J. Neuroradiol. 2013;34:1326–33.

31. Zonari P, Baraldi P, Crisi G. Multimodal MRI in the characterization of glial neoplasms: the combined role of single-voxel MR spectroscopy, diffusion imaging and echo-planar perfusion imaging. Neuroradiology 2007;49:795–803.

32. Verma R, Zacharaki EI, Ou Y, Cai H, Chawla S, Lee S-K, Melhem ER, Wolf R, Davatzikos C. Multiparametric tissue characterization of brain neoplasms and their recurrence using pattern classification of MR images. Acad. Radiol. 2008;15:966–77.

33. Di Costanzo A, Scarabino T, Trojsi F, Giannatempo GM, Popolizzio T, Catapano D, Bonavita S, Maggialetti N, Tosetti M, Salvolini U, D'Angelo VA, Tedeschi G. Multiparametric 3T MR approach to the assessment of cerebral gliomas: tumor extent and malignancy. Neuroradiology 2006;48:622–31.

34. Louis DN, Holland EC, Cairncross JG. Glioma Classification. Am. J. Pathol. 2001;159:779–786.

35. Muti M, Aprile I, Principi M, Italiani M, Guiducci A, Giulianelli G, Ottaviano P. Study on the variations of the apparent diffusion coefficient in areas of solid tumor in high grade gliomas. Magn. Reson. Imaging 2002;20:635–41.

36. Sajda P, Du S, Brown TR, Stoyanova R, Shungu DC, Mao X, Parra LC. Nonnegative matrix factorization for rapid recovery of constituent spectra in magnetic resonance chemical shift imaging of the brain. IEEE Trans. Med. Imaging 2004;23:1453–65.

37. Ortega-Martorell S, Lisboa PJG, Vellido A, Simões RV, Pumarola M, Julià-Sapé M, Arús C. Convex non-negative matrix factorization for brain tumor delimitation from MRSI data. PloS One 2012;7:e47824.

38. Dynamic Susceptibility Contrast MR ANalysis (DSCoMAN). Available at: https://dblab.duhs.duke.edu/modules/dscoman/index.php?id=1

39. Schneider CA, Rasband WS, Eliceiri KW. NIH Image to ImageJ: 25 years of image analysis. Nat. Methods 2012;9:671–675.

40. Boxerman JL, Schmainda KM, Weisskoff RM. Relative cerebral blood volume maps corrected for contrast agent extravasation significantly correlate with glioma tumor grade, whereas uncorrected maps do not. AJNR Am. J. Neuroradiol. 2006;27:859–67.

41. Van Cauter S, Sima DM, Luts J, ter Beek L, Ribbens A, Peeters RR, Osorio Garcia MI, Li Y, Sunaert S, Van Gool S, Van Huffel S, Himmelreich U. Reproducibility of rapid short echo time CSI at 3 tesla for clinical applications. J. Magn. Reson. Imaging JMRI 2013;37:445–56.

42. Ogg RJ, Kingsley PB, Taylor JS. WET, a T1- and B1-insensitive water-suppression method for in vivo localized 1H NMR spectroscopy. J. Magn. Reson. B 1994;104:1–10.

43. Poullet J-B, Quantification and classification of magnetic resonance spectroscopic data for brain tumor diagnosis. PhD Thesis, Leuven, 2008. Available at: http://homes.esat.kuleuven.be/~biomed/software.php#SpidGUI

44. Croitor Sava AR, Sima DM, Poullet J-B, Wright AJ, Heerschap A, Van Huffel S. Exploiting spatial information to estimate metabolite levels in two-dimensional MRSI of heterogeneous brain lesions. NMR Biomed. 2011;24:824–35.

45. Poullet J-B, Sima DM, Van Huffel S, Van Hecke P. Frequency-selective quantitation of short-echo time 1H magnetic resonance spectra. J. Magn. Reson. San Diego Calif 1997 2007;186:293–304.

46. Andersson J, Xu J, Yacoub E. A comprehensive Gaussian process framework for correcting distortions and movements in diffusion images. In: Proceedings of the 20th Annual Meeting of ISMRM. ; 2012.

47. Veraart J, Sijbers J, Sunaert S, Leemans A, Jeurissen B. Weighted linear least squares estimation of diffusion MRI parameters: strengths, limitations, and pitfalls. NeuroImage 2013;81:335–346.

48. Le Bihan D, Mangin JF, Poupon C, Clark CA, Pappata S, Molko N, Chabriat H. Diffusion tensor imaging: concepts and applications. J. Magn. Reson. Imaging JMRI 2001;13:534–46.

49. Statistical Parametric Mapping (SPM). Available at: http://www.fil.ion.ucl.ac.uk/spm/

50. Maes F, Collignon A, Vandermeulen D, Marchal G, Suetens P. Multimodality image registration by maximization of mutual information. IEEE Trans. Med. Imaging 1997;16:187–98.

51. Leemans A, Jeurissen B, Sijbers J, Jones D. ExploreDTI: a graphical toolbox for processing, analyzing, and visualizing diffusion MR data. In: 17th Annual Meeting of Intl Soc Mag Reson Med. Hawaï, USA; 2009. p. 3537.

52. Lee DD, Seung HS. Learning the parts of objects by non-negative matrix factorization. Nature 1999;401:788–91.

53. Gillis N, Glineur F. Accelerated multiplicative updates and hierarchical ALS algorithms for nonnegative matrix factorization. Neural Comput. 2012;24:1085–105.

54. Li Y, Sima D, Van Cauter S, Himmelreich U, Pi Y, Van Huffel S. Simulation study of tissue type differentiation using non-negative matrix factorization. In: Proceedings of BIOSIGNALS 2012. Algarve, Portugal; 2012. pp. 212–217.

55. Seber G. Multivariate Observations. Hoboken, NJ: John Wiley & Sons, Inc.; 1984.

56. Mazzara GP, Velthuizen RP, Pearlman JL, Greenberg HM, Wagner H. Brain tumor target volume determination for radiation treatment planning through automated MRI segmentation. Int. J. Radiat. Oncol. Biol. Phys. 2004;59:300–12.

57. Gordillo N, Montseny E, Sobrevilla P. State of the art survey on MRI brain tumor segmentation. Magn. Reson. Imaging 2013;31:1426–38.

58. Menze B, Jakab A, Bauer S, Kalpathy-Cramer J, Farahani K, Kirby J, Burren Y, Porz N, Slotboom J, Wiest R, Lanczi L, Gerstner E, Weber MA, Arbel T, Avants B, Ayache N, Buendia P, Collins L, Cordier N, Corso J, Criminisi A, Das T, Delingette H, Demiralp C, Durst C, Dojat M, Doyle S, Festa J, Forbes F, Geremia E, Glocker B, Golland P, Guo X, Hamamci A, Iftekharuddin K, Jena R, John N, Konukoglu E, Lashkari D, Antonio Mariz J, Meier R, Pereira S, Precup D, Price SJ, Riklin-Raviv T, Reza S, Ryan M, Schwartz L, Shin HC, Shotton J, Silva C, Sousa N, Subbana N, Szekely G, Taylor T, Thomas O, Tustison N, Unal G, Vasseur F, Wintermark M, Hye Ye D, Zhao L, Zikic D, Prastawa M, Reyes M, Van

Leemput K. The Multimodal Brain Tumor Image Segmentation Benchmark (BRATS). 2014; hal-00935640, version 2.

59. Li Y, Sima DM, Van Cauter S, Himmelreich U, Croitor Sava AR, Pi Y, Liu Y, Van Huffel S. Unsupervised nosologic imaging for glioma diagnosis. IEEE Trans. Biomed. Eng. 2013;60:1760–3.

60. Laudadio T, Martínez-Bisbal MC, Celda B, Van Huffel S. Fast nosological imaging using canonical correlation analysis of brain data obtained by two-dimensional turbo spectroscopic imaging. NMR Biomed. 2008;21:311–21.

61. Du S, Mao X, Sajda P, Shungu DC. Automated tissue segmentation and blind recovery of (1)H MRS imaging spectral patterns of normal and diseased human brain. NMR Biomed. 2008;21:33–41.

62. Li Y, Sima DM, Cauter SV, Croitor Sava AR, Himmelreich U, Pi Y, Van Huffel S. Hierarchical non-negative matrix factorization (hNMF): a tissue pattern differentiation method for glioblastoma multiforme diagnosis using MRSI. NMR Biomed. 2013;26:307–19.

63. Weber M-A, Henze M, Tüttenberg J, Stieljes B, Meissner M, Zimmer F, Burkholder I, Kroll A, Combs SE, Vogt-Schaden M, Giesel F, Zoubaa S, Haberkorn U, Kauczor HU, Essig M. Biopsy targeting gliomas: do functional imaging techniques identify similar target areas? Invest. Radiol. 2010;45:755–68.

Table legends

Table 1: Average, standard deviation and range of the Dice-scores for the gliomas without necrosis. Results are reported for the full MP-MRI dataset (underlined), MP-MRI without cMRI, PWI, MRSI and DKI and for cMRI data only.

Table 2: Average, standard deviation and range of the correlation coefficients for the gliomas without necrosis. Results are reported for the full MP-MRI dataset (underlined), MP-MRI without cMRI, PWI, MRSI and DKI and for cMRI data only.

Table 3: Average, standard deviation and range of the Dice-scores for the GBM (grade IV) patients. Results are reported for the active tumor, necrotic and whole tumor region using the full MP-MRI dataset (underlined), MP-MRI without cMRI, PWI, MRSI and DKI and for cMRI data only.

Table 4: Average, standard deviation and range of the correlation coefficients for the GBM patients. Results are reported for the active tumor and necrotic region using the full MP-MRI dataset (underlined), MP-MRI without cMRI, PWI, MRSI and DKI and for cMRI data only.

Table1

	Dice-score tumor [%]					
	All	No cMRI	No PWI	No MRSI	No DKI	cMRI only
Average	**86**	**75**	**84**	**84**	**83**	**81**
Standard deviation	**13**	**19**	**14**	**16**	**16**	**18**
Range [Min;Max]	**[50;96]**	**[42;95]**	**[52;97]**	**[41;96]**	**[46;97]**	**[38;96]**

Table2

	Correlation coefficient tumor					
	All	No cMRI	No PWI	No MRSI	No DKI	cMRI only
Average	**0.96**	**0.92**	**0.97**	**0.98**	**0.98**	**0.96**
Standard deviation	**0.07**	**0.13**	**0.08**	**0.02**	**0.02**	**0.05**
Range [Min;Max]	**[0.75;1]**	**[0.57;1]**	**[0.72;1]**	**[0.93;1]**	**[0.94;1]**	**[0.82;1]**

Table3

	Dice-score active tumor [%]						Dice-score necrosis [%]						Dice-score whole tumor [%]					
	All	No cMRI	No PWI	No MRSI	No DKI	cMRI only	All	No cMRI	No PWI	No MRSI	No DKI	cMRI only	All	No cMRI	No PWI	No MRSI	No DKI	cMRI only
Average	**77**	**63**	**72**	**68**	**76**	**67**	**71**	**57**	**68**	**66**	**67**	**48**	**85**	**77**	**80**	**78**	**82**	**69**
Standard deviation	**9**	**11**	**20**	**16**	**11**	**16**	**23**	**25**	**25**	**26**	**26**	**23**	**12**	**15**	**19**	**18**	**13**	**17**
Range [Min;Max]	**[59;88]**	**[44;84]**	**[20;88]**	**[43;90]**	**[58;92]**	**[38;87]**	**[23;95]**	**[18;86]**	**[19;96]**	**[25;95]**	**[22;94]**	**[27;92]**	**[54;98]**	**[40;92]**	**[36;98]**	**[40;98]**	**[48;92]**	**[39;95]**

Table4

	Correlation coefficient active tumor						Correlation coefficient necrosis					
	All	No cMRI	No PWI	No MRSI	No DKI	cMRI only	All	No cMRI	No PWI	No MRSI	No DKI	cMRI only
Average	**0.90**	**0.91**	**0.87**	**0.83**	**0.95**	**0.85**	**0.97**	**0.92**	**0.97**	**0.96**	**0.96**	**0.93**
Standard deviation	**0.10**	**0.06**	**0.14**	**0.16**	**0.05**	**0.17**	**0.03**	**0.13**	**0.03**	**0.06**	**0.04**	**0.09**
Range [Min;Max]	**[0.71;0.99]**	**[0.76;0.98]**	**[0.63;0.99]**	**[0.54;0.99]**	**[0.81;0.99]**	**[0.59;0.99]**	**[0.90;1]**	**[0.58;0.99]**	**[0.90;0.99]**	**[0.81;1]**	**[0.87;0.99]**	**[0.70;0.99]**

Figure legends

Figure 1: Schematic overview of the hNMF procedure.

Figure 2: Coregistered MRI maps of different modalities for GBM patient 16: T2 (A), T1+C (B), MD (C), MK (D), rCBV (E), Cho (F), Cre (G) and Lip maps (H). The green box indicates the MRSI ROI.

Figure 3: Results of the hNMF analysis for GBM patient 16: abundance maps for active tumor (A), necrosis (B), edema (C), white matter (D) and blood vessels (E), and error map (F). Comparison of the segmentation obtained with hNMF (in blue) and the manual delineation of the radiologist (in green) is given for active tumor (G) and for necrosis (H). The hNMF sources are shown in I.

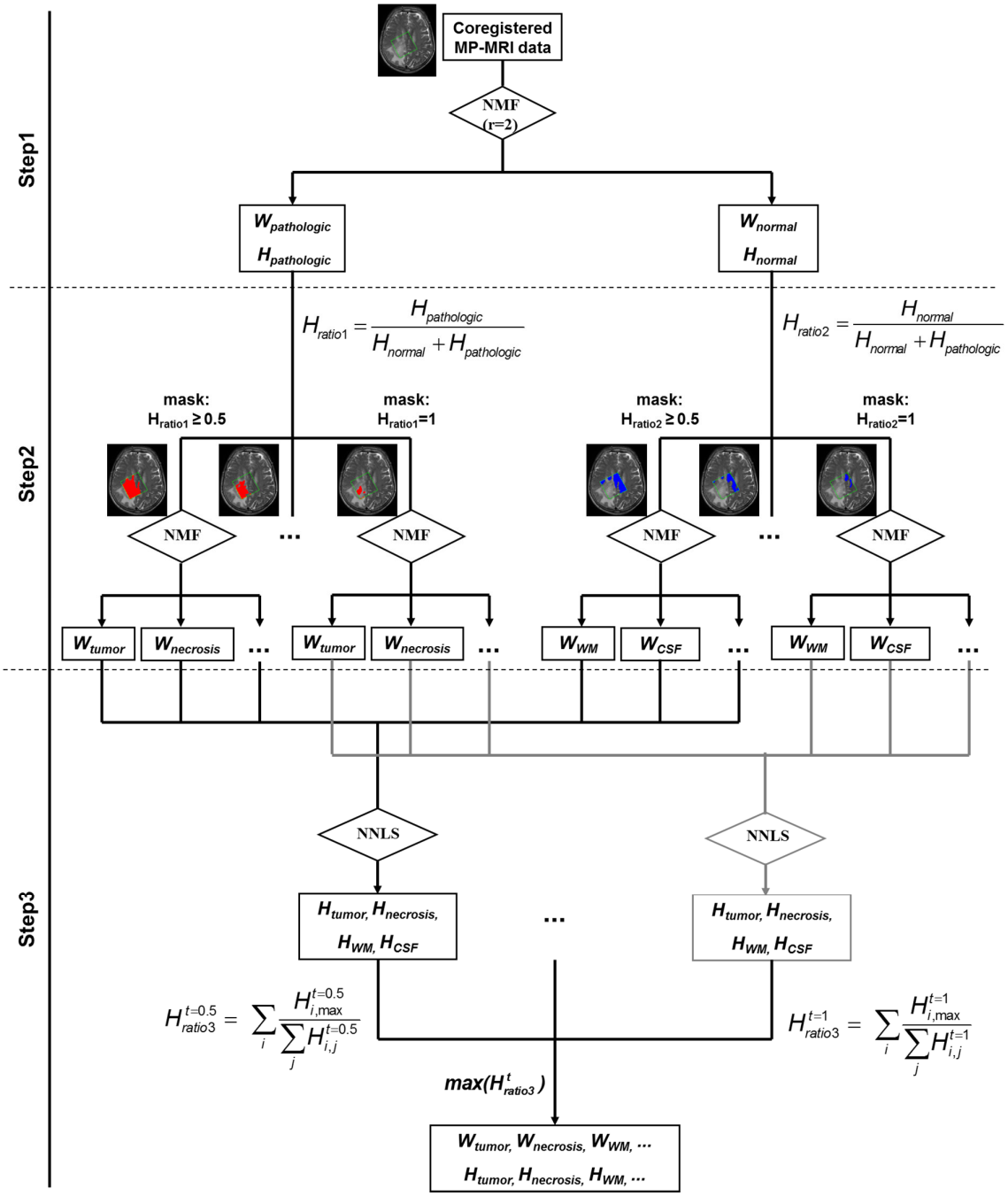

Step1
Step2
Step3
Coregistered MP-MRI data
NMF (r=2)
$W_{pathologic}$ $H_{pathologic}$
W_{normal} H_{normal}
$H_{ratio1} = \frac{H_{pathologic}}{H_{normal} + H_{pathologic}}$
$H_{ratio2} = \frac{H_{normal}}{H_{normal} + H_{pathologic}}$
mask: $H_{ratio1} \geq 0.5$
mask: $H_{ratio1}=1$
mask: $H_{ratio2} \geq 0.5$
mask: $H_{ratio2}=1$
NMF
W_{tumor} $W_{necrosis}$
W_{WM} W_{CSF}
NNLS
$H_{tumor}, H_{necrosis}, H_{WM}, H_{CSF}$
$H_{ratio3}^{t=0.5} = \sum_i \frac{H_{i,\max}^{t=0.5}}{\sum_j H_{i,j}^{t=0.5}}$
$H_{ratio3}^{t=1} = \sum_i \frac{H_{i,\max}^{t=1}}{\sum_j H_{i,j}^{t=1}}$
$max(H_{ratio3}^{t})$
$W_{tumor}, W_{necrosis}, W_{WM}, \cdots$
$H_{tumor}, H_{necrosis}, H_{WM}, \cdots$

Figure 1

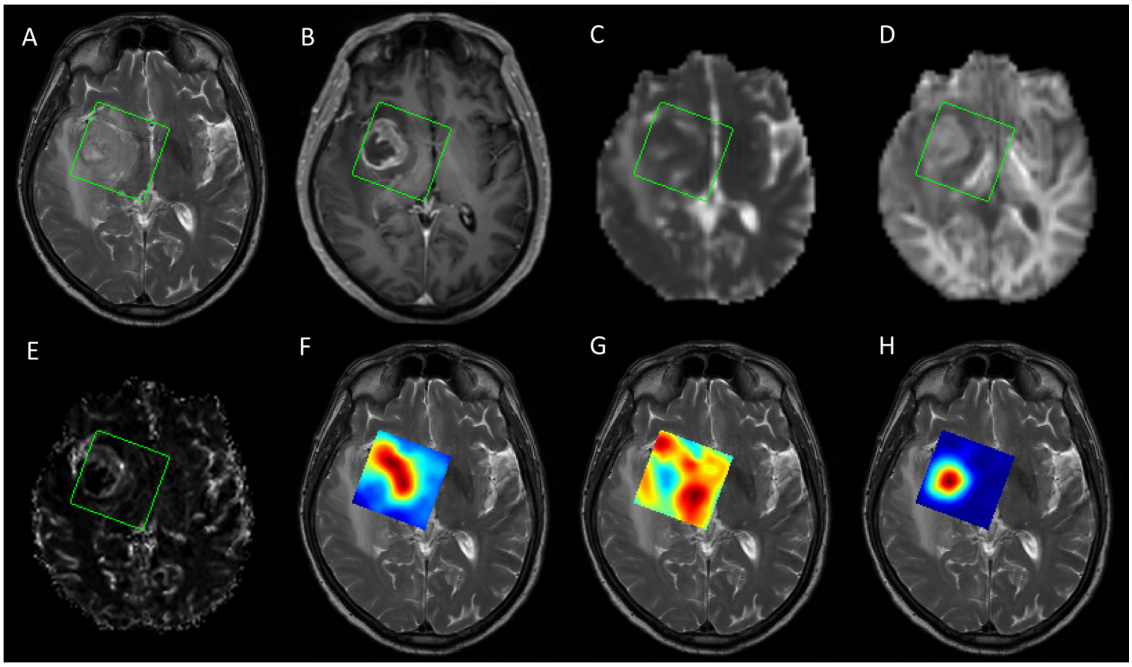


Figure 2

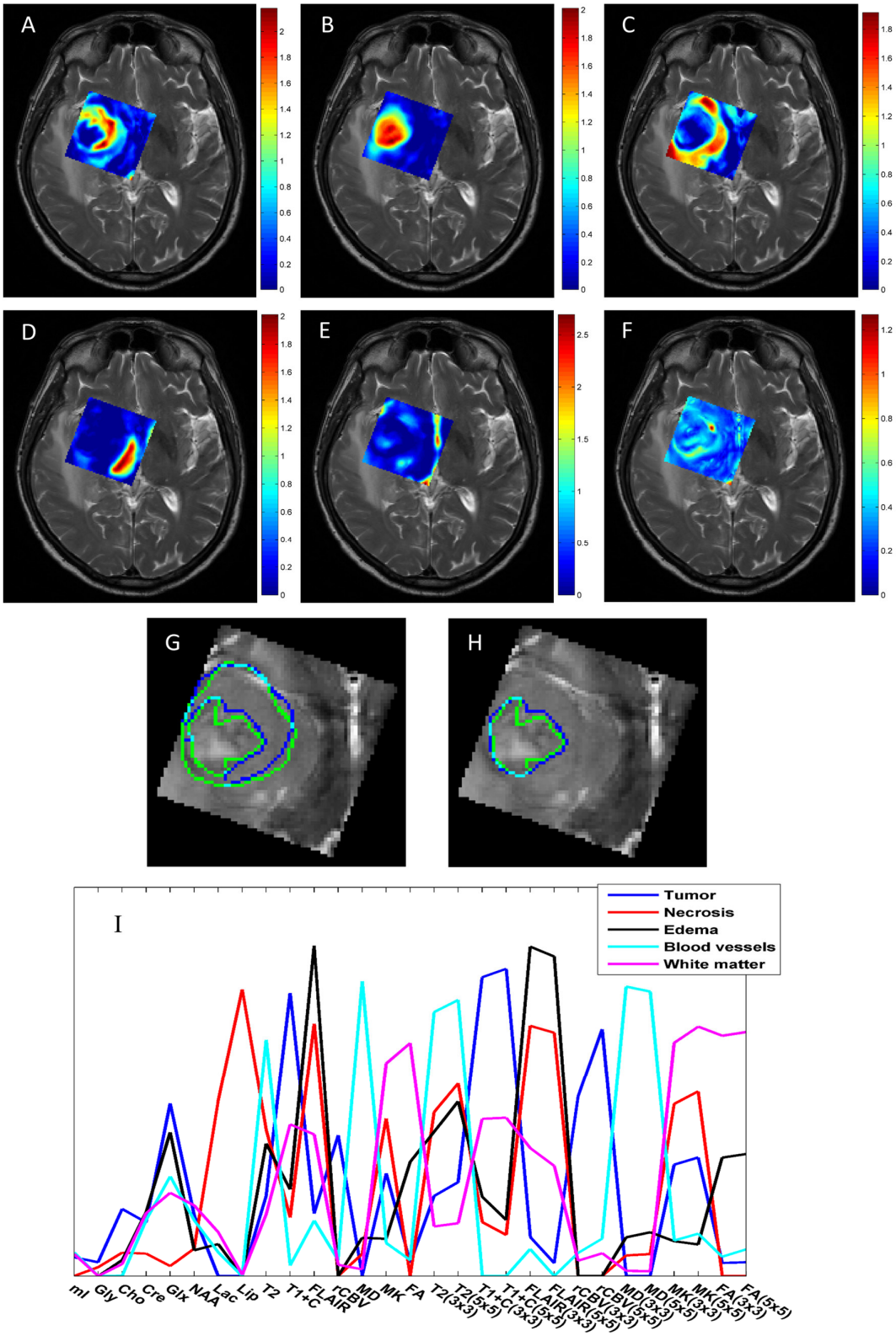

A
B
C
D
E
F
G
H
I
Tumor
Necrosis
Edema
Blood vessels
White matter
ml
Gly
Cho
Cre
Glx
NAA
Lac
Lip
T2
T1+C
FLAIR
rCBV
MD
MK
FA
T2(3x3)
T2(5x5)
T1+C(3x3)
T1+C(5x5)
FLAIR(3x3)
FLAIR(5x5)
rCBV(3x3)
rCBV(5x5)
MD(3x3)
MD(5x5)
MK(3x3)
MK(5x5)
FA(3x3)
FA(5x5)

Figure 3